PASJ: Publ. Astron. Soc. Japan **58**, 703–718, 2006 August 25
© 2006. Astronomical Society of Japan.

Non-Uniform Temperature Distribution in the Galaxy Clusters 2A 0335+096 and Abell 496 Observed by XMM-Newton

Takeshi TANAKA, Hideyo KUNIEDA, and Murat HUDAVERDI
Department of Physics, Nagoya University, Furo-cho, Chikusa-ku, Nagoya 464-8602
ttanaka@u.phys.nagoya-u.ac.jp
and
Akihiro FURUZAWA and Yuzuru TAWARA
EcoTopia Science Institute, Nagoya University, Furo-cho, Chikusa-ku, Nagoya 464-8602

(Received 2006 April 22; accepted 2006 June 1)

Abstract

We present the XMM-Newton results of the galaxy clusters 2A 0335+096 and A 496. From an investigation of 2-dimensional ICM profiles, we obtained new features related to dynamical activities in the ICM. In 2A 0335+096, we found a spiral cool tail around the central cold core, which is trailing from the opposite side of the cold front observed by Chandra. The deprojected temperature of the tail is 1.7 keV. The spiral feature apparently shows a turnaround motion of the core. We suggest that the cool tail feature represents evidence for turbulent viscous stripping of the remaining subcluster core. For A 496, we found another cold front 4′ south of the X-ray emission peak. From the pressure profile across the cold front, we derived an upper limit to the Mach number of a gas body of 0.2. Regarding the temperature distribution in the outer region, we found non-uniformity on the cluster scale for both clusters, which suggests that both clusters experienced a merger in the past. We argue that the gas dynamical motions seen in the central regions of both clusters can be attributed to the past merger.

Key words: galaxies: clusters: general — galaxies: clusters: individual (2A 0335+096, Abell 496) — galaxies: intergalactic medium — X-rays: galaxies: clusters

1. Introduction

Clusters of galaxies are the largest gravitationally-bound systems in the Universe, and are seen at intersections of galaxy filaments in the large-scale structure. As predicted by the scenario of structure formation in the Universe, clusters of galaxies grow dynamically by merging with one another and accreting smaller systems, such as groups of galaxies. A non-uniform temperature distribution due to the activities was revealed by ASCA (Tanaka et al. 1994) for many clusters (e.g., Watanabe et al. 1999, 2001; Churazov et al. 1999; Furusho et al. 2001).

So far, Chandra and XMM-Newton observations have improved our understanding of a cluster of galaxies. The XMM-Newton spectroscopy of bright cold cores has revealed that the amount of cool gas at lower temperatures is much smaller than predicted by the standard isobaric cooling flow model (e.g., Tamura et al. 2001a; Kaastra et al. 2001; Peterson et al. 2001). Several explanations for the lack of the cool gas have been given by many authors. Chandra, with unprecedented angular resolution and sensitivities in wider energy bands than ROSAT, has enabled us to derive the velocity of a gas body. A study of gas profiles across an arclike brightness edge (cold front) showed that the cold dense core is moving at subsonic speed (e.g., Markevitch et al. 2000; Vikhlinin et al. 2001; Mazzotta et al. 2001). Markevitch et al. (2000) suggested that the cold front is the leading edge of the remaining core of a merged subcluster.

The cold front feature is not unique to merging clusters. Markevitch, Vikhlinin, and Forman (2003) found that Chandra images for 25 of 37 clusters, which were known to be relaxed clusters by earlier studies, exhibit the brightness edge around a central core. Taking into account the projection effect, an even larger fraction of clusters is expected to have a cold front. It is thus likely that the dynamical motion of the cold core is a common feature even for clusters that do not exhibit merger activity. For morphologically relaxed clusters, alternative hypotheses have been proposed to explain the motion of the core. Mazzotta et al. (2001) suggested the hypothesis that the cold front is the result of the oscillation of a subhalo due to the collapse of two different perturbations in the primordial density field. Another model proposed by Tittley and Henriksen (2005) is that the core oscillation is triggered by the off-axis passage of a subcluster. Since both core-oscillation models do not predict a temperature variation on a cluster scale, an investigation of the 2-dimensional (2D) temperature profile would tell which model is plausible.

In this paper we report on the XMM-Newton (Jansen et al. 2001) results of nearby X-ray bright clusters 2A 0335+096 ($z = 0.0349$) and A 496 ($z = 0.0329$). Both of the clusters were recognized as being relaxed clusters with the cooling flow phenomenon. As a signature of the cooling flow phenomenon, filaments of the Hα-emitting gas surrounding a central giant elliptical galaxy were observed by Romanishin and Hintzen (1988) for 2A 0335+096 and Fabian et al. (1981) for A 496. Previous X-ray observations of smooth morphology on large scales and a bright cold core also recognized both of the clusters to be dynamically relaxed. Contrary to long-standing claims of the relaxation, Chandra observations revealed a dynamical motion of the cold core. For 2A 0335+096,

Downloaded from https://academic.oup.com/pasj/article/58/4/703/1456709 by Yildiz Teknik University Library (YTU) user on 25 February 2022

Mazzotta, Edge, and Markevitch (2003) presented complex structures including a cold front, and argued that the cold core is moving toward the south with a Mach number of $M \simeq 0.8 \pm 0.2$. For A 496, there are three brightness edges seen $\sim 1'.5$ north-northwest, $\sim 50''$ south-southwest, and $\sim 20''$ east of the X-ray peak (Tittley, Henriksen 2005). Dupke and White (2003) studied gas profiles across the northern edge, and found that they are consistent with cold-front features. Based on the central morphology, Tittley and Henriksen (2005) argued that these edges can be explained by their core-oscillation model.

XMM-Newton observations of both clusters have also been presented by Werner et al. (2006) for 2A 0335+096 and Tamura et al. (2001b) for A 496. Werner et al. (2006) investigated the temperature and metallicity distributions by employing a multi-temperature model, *wdem* model, which is an empirical approximation for the spectrum in cold cores of clusters of galaxies (Kaastra et al. 2004; de Plaa et al. 2004). The radial profiles obtained by the multi-temperature *wdem* model showed that the gas temperature drops in the core, while the elemental abundances peak at the center, and gradually decrease toward the outside. Using the derived elemental abundances, they estimated the relative numbers of SNe Ia and SNe II for the metal-enrichment of the ICM. For 2D ICM profiles, they confirmed the central asymmetric temperature distribution found by Chandra and showed a similar asymmetry of the iron abundance distribution. Werner et al. (2006) suggested that the cold central core is the surviving core of a merged subcluster. In this paper we present a cool tail feature around the central core and a large-scale non-uniform temperature distribution in the outer region. For A 496, Tamura et al. (2001b) presented radial profiles of the gas temperature and the metallicity for various elements, and discussed the radial contributions of SNe Ia and SNe II. They also investigated the temperature structure in the cool central region utilizing the Reflection Grating Spectrometer (RGS), and found an absence of emission from gas cooler than ~ 1 keV, which is expected by a standard cooling flow model. In this paper we report on the discovery of another cold front and a non-uniform temperature distribution at the outside.

Throughout this paper we assume $H_0 = 70\,\mathrm{km\,s^{-1}\,Mpc^{-1}}$, $\Omega_0 = 0.27$, and $\Lambda_0 = 0.73$. For 2A 0335+096, $1'$ corresponds to 41.7 kpc, and for A 496 it is 39.4 kpc. We use the solar abundance table given by Anders and Grevesse (1989).

2. Observation and Data Reduction

We analyzed XMM-Newton archival data. For 2A 0335+096, it was observed three times with XMM-Newton. We used only the data of the 2nd observation because the other observations were significantly affected by soft proton flares. Observation ID of the data are listed in table 1 along with the observation date.

The thin filter was used in all European Photon Imaging Camera (EPIC) observations for both clusters. The EPIC MOS cameras (Turner et al. 2001) were operated in the full-frame mode in all observations, whereas the EPIC pn camera (Strüder et al. 2001) was operated in the full-frame mode for 2A 0335+096 and in the extended full-frame mode for A 469. The RGS (den Herder et al. 2001) was operated in the spectroscopy mode. Since detailed RGS results of A 496 have already been reported by Tamura et al. (2001b), we present RGS results for 2A 0335+096 only. For 2A 0335+096, the RGS dispersion axis was oriented at a position angle of 74° (north to east).

Table 1. Log of XMM-Newton observations of 2A 0335+096, A 496, and fields used to produce the blank-sky background data.

Target	Obs. ID	Date	Net exposure time (ks)		
			MOS1	MOS2	pn
2A 0335+096	0147800201	2003-08-04	102.4	103.8	90.5
Abell 496	0135120201*	2001-02-01	14.3	14.0	7.4
Deep Field 1334+37	0109660801	2001-06-12	39.1	···	27.9
Deep Field 1334+37	0109661001	2001-06-23	57.5	57.6	47.4
Hubble Deep Field N	0111550101	2001-05-18	38.1	38.4	33.5
Hubble Deep Field N	0111550201	2001-05-18	33.4	32.5	26.1
Hubble Deep Field N	0111550401	2001-06-01	83.0	83.9	66.6
SDS-5	0112370601	2002-08-12	29.4	30.3	24.6
SDS-6	0112370701	2002-08-08	47.2	47.5	41.2
SDS-7	0112370801	2002-08-09	33.5	34.1	27.7
SDS-1	0112371001	2000-08-02	38.0	38.3	30.2
GRB 030329	0128531601	2003-12-12	68.2	69.1	48.8
AXAF Ultra Deep F	0108062101*	2002-01-20	41.0	41.6	33.3
AXAF Ultra Deep F	0108062301*	2002-01-23	73.4	73.4	60.4
XMDSOM_1	0109520101*	2002-01-29	25.2	25.5	19.0
XMDSOM_3	0109520301*	2002-02-02	21.7	21.7	15.8
XMDSOM_5	0109520501*	2001-07-03	23.7	24.0	17.7
XMDS SSC_3	0111110301*	2001-07-03	21.3	20.4	16.5
XMDS SSC_4	0111110401*	2001-07-03	27.2	26.6	18.4

* Observation mode of the pn is "Extended Full Frame".

Downloaded from https://academic.oup.com/pasj/article/58/4/703/1456709 by Yildiz Teknik University Library (YTU) user on 25 February 2022

We processed the observation data files and created calibrated event files using the SAS version 6.1.0. In the standard analysis, events with the pattern ≤ 4 (12) and the expression of FLAG==0 (#XMMEA_EM) are used for the pn (MOS). However, for the pn data of 2A 0335 + 096 we selected only single events because the double-event spectra showed a systematic blue shift of 30–40 eV for the instrumental emission lines seen in the 7–9 keV range. This is probably a gain-related problem that was not cleared up during the XMM-Newton SOC data processing.

First, the time-intervals of the soft proton flares must be excluded. It is known that a high-energy band is more sensitive to flare events than a soft-energy band. We thus chose 8–12 keV and 10–20 keV events as indicators of the flaring time for the MOS and pn, respectively. We then made frequency distributions against the counting rate for each light curve, which is represented by a narrow Gaussian model. We excluded time-intervals that deviated from the average counting rate by more than the Gaussian 2.5σs. The resulting net exposures are given in table 1. For the RGS we used the same selection criteria as performed on background data sets constructed by Tamura, den Herder, and González-Riestra (2003).[1] The net exposure for both RGSs was 101.7 ks.

Since the X-ray emissions from both 2A 0335 + 096 and A 496 extend over the fields of view of the EPIC detectors, we needed to use the blank-sky background. Referring to Read and Ponman (2003), we collected observations that did not contain extragalactic extended sources, and produced background event files. High background periods were excised as was done for the two clusters, and point sources were removed. The observations used to produce the blank-sky background data as well as the net exposure times are also listed in table 1. In order to correct for any long-term variation of the stable background (e.g., Katayama et al. 2004), we used a data set taken with the filter wheel in the closed position. We added events of the filter-closed data to the blank-sky events so that the counting rate of 10–12 keV (12–14 keV) for the MOS (pn) would be equal between the observation of our clusters and the resulting background. Since the cluster's central bright emission contaminates even those high-energy bands, we compared the counting rate of the spectrum of the outer region of $r > 7'$.

For the RGS background we used the blank-sky data sets produced by the instrument team (Tamura et al. 2003).[1] According to Tamura, den Herder, and González-Riestra (2003),[1] the rms deviations of the background from the average are less than 30% over the full energy range. We thus assigned systematic errors of 30% to the background spectra in our analysis.

3. 2A 0335 + 096

3.1. X-Ray Morphology

Figure 1 shows the contours from the combined MOS images in the 0.5–10 keV energy band, overlaid on the DSS optical image. The X-ray image, binned to pixels of 4.″1, was corrected for the background, exposure time, and vignetting.

[1] ⟨http://xmm.vilspa.esa.es/docs/documents/CAL-TN-0034-1-0.ps.gz⟩.

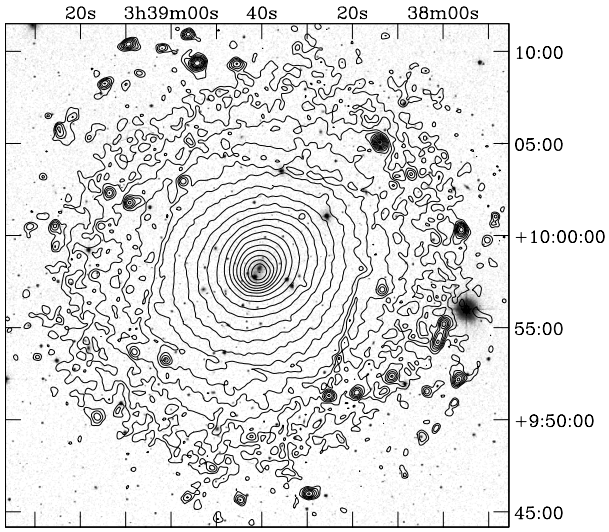


Fig. 1. Contours of the smoothed 0.5–10 keV MOS image, overlaid on the DSS optical image for 2A 0335 + 096. The X-ray image of 4.″1 pixels was corrected for the background, exposure, and vignetting. The spacing factor between the contours is 0.7. The smoothing function is a Gaussian with $\sigma = 8.''2$.

The smoothing function is a Gaussian with $\sigma = 8.''2$. The spacing factor between the contours is 0.7. As reported in the ROSAT observation of this cluster (Irwin, Sarazin 1995), the overall X-ray emission is slightly elongated in northwesterly and southeasterly directions. Note that two optical bright sources seen at $r < 30''$ are the D galaxy for the northwest source and a foreground star for the southeast source. A Chandra observation revealed a number of blobs and/or filaments in the central region. A comparison of the Chandra and optical images shows that the brightest blobs are located between the D galaxy and the foreground star (Mazzotta et al. 2003). In figure 1, one can also notice that the X-ray brightness distribution in the central region exhibits a deviation from spherical symmetry. At $r \sim 1'$ south of the X-ray peak there exists a steep brightness gradient, which corresponds to the cold front observed by Chandra. The cold front indicates that the cold core is moving toward the south with a Mach number of $M \simeq 0.8 \pm 0.2$ (Mazzotta et al. 2003). In addition, the central brightness distribution is more extended in a northwesterly direction. The brightness extension implies that the core came from the northwest.

Figure 2 shows the surface brightness profiles in the energy ranges 0.5–10 keV, 1–2 keV, and 2–10 keV. The profiles were extracted from the combined MOS and pn images, which were corrected for the background, exposure, and vignetting. It is obviously clear that the surface brightness in the soft energy band is more centrally concentrated than in the hard energy band. This indicates the presence of a cool component toward the cluster center.

As mentioned before, the X-ray surface brightness distribution is not symmetric around its X-ray peak. In order to emphasize the asymmetric structure, we examined the deviation of the surface brightness from the azimuthally averaged value, which corresponds to the radial profile shown in figure 2. Figure 3 shows the distribution of the ratio of the surface brightness

Downloaded from https://academic.oup.com/pasj/article/58/4/703/1456709 by Yildiz Teknik University Library (YTU) user on 25 February 2022

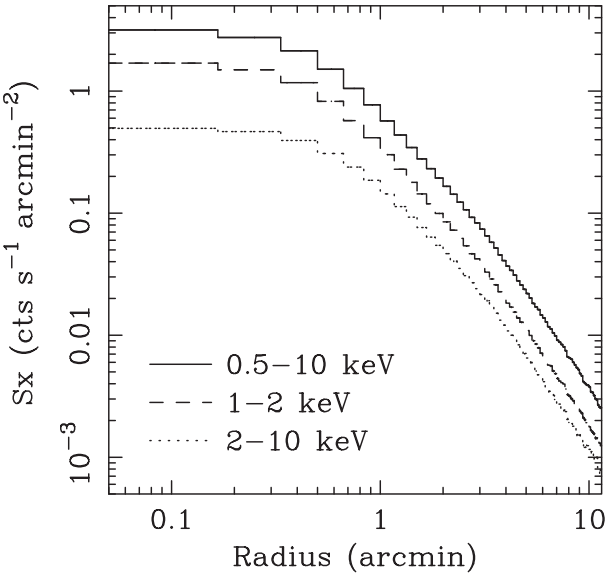


Fig. 2. Surface brightness profiles of 2A 0335+096 in the energy ranges 0.5–10 keV, 1–2 keV, and 2–10 keV from the top to the bottom, made from the combined MOS and pn images that were corrected for the background, exposure, and vignetting.

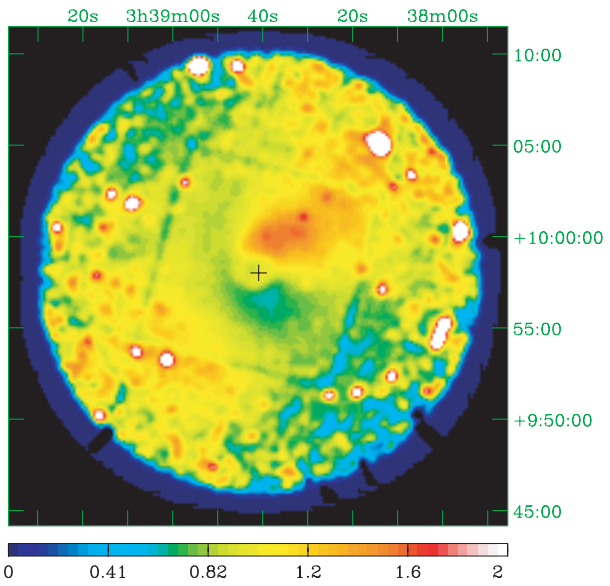


Fig. 3. Relative deviation of the 0.5–10 keV MOS surface brightness from the azimuthally averaged value for 2A 0335+096. The cross shows the position of the X-ray brightness peak, from which the averaged value was derived.

to the averaged value at each radius. The map with a pixel size of 8.″2 was filtered with a $\sigma = 1.5$ pixels Gaussian. The cross mark on the map shows the position of the X-ray brightness peak, from which the averaged value was derived. The round white regions, where the color map is saturated, correspond to point sources. The outstanding point source located $\sim 9.'7$ northwest of the X-ray emission peak has been identified with the Narrow Angle Tail radio galaxy in this cluster (Irwin, Sarazin 1995; Sarazin et al. 1995). For cluster substructures, there are two prominent excess regions seen $r \gtrsim 1'$ northwest of the X-ray peak and $r \gtrsim 4'$ southeast of the X-ray peak. The excess regions apparently show the central brightness extension toward the northwest and the overall brightness elongation in northwesterly and southeasterly directions.

3.2. *Radial Profiles*

For spectral fits, we utilized the XSPEC v11.3.1 package and employed the APEC model (Smith et al. 2001) as a spectral model for collisionally-ionized diffuse gas. Best-fit parameters for a region were obtained from simultaneous fits to the combined MOS1 and MOS2 spectrum and the pn spectrum. The used energy band for the simultaneous fits was 0.5–10 keV, unless otherwise mentioned. In order to take into account the remaining calibration uncertainties, we applied the systematic error adopted from Kaastra et al. (2004). The applied systematic errors are 5% in the 0.5–2 keV energy range and 10% in the 2–10 keV energy range relative to the source flux.

To investigate the radial profiles of the temperature and metallicity, we extracted the MOS and pn spectra from 14 annular regions in the range of $r = 0'$–$11.'5$. Point sources were excluded before the extraction of a spectrum, and the annuli were chosen such that each width would be larger than $30''$ in consideration of the point-spread function. Below ~ 1 keV, the sky background is significantly affected by the soft X-rays from the local environment (Hot Bubbles) around the solar system, which are diffuse, but highly anisotropic. In addition, the photoelectric absorption of the soft X-rays by our galaxy's interstellar medium becomes significant. Therefore, for spectral fits below ~ 1 keV we excluded the energy range where the estimated background was more than $\sim 25\%$ of the source flux. Since we lose the restriction on the absorption parameter through the exclusion, the absorptions for the outer annuli of $r > 5'$ were fixed at 2.4×10^{21} cm^{-2}, referred to the results for the inner annuli. For the pn spectra from the outside region of $r > 6'$, we also excluded the energy range above 7.5 keV, where the instrumental fluorescent lines of Ni, Cu, and Zn could not be subtracted appropriately.

As the first attempt, we fitted the annular spectra with an absorbed single-temperature (1T) model. The free parameters were the temperature, metallicity, normalization, and the hydrogen column density. The results of the fits are shown in figure 4. The model gives acceptable fits for the outer 11 annuli, as recognized by the distribution of the reduced χ^2. The temperature profile shows a strong drop, from ~ 3.3 keV between $r = 3'$–$6'$ to ~ 1.9 keV at the center, which is consistent with the result of Werner et al. (2006), while the metallicity profile shows an increase toward the center, from 0.37 solar at $r \sim 6'$ to 0.65 solar at $r < 1'$. The hydrogen column density profile shows a higher absorption of $(2.3$–$2.5) \times 10^{21}$ cm^{-2} compared with the Galactic value of $(1.7$–$1.8) \times 10^{21}$ cm^{-2} from the 21 cm measurement (Dickey, Lockman 1990). Note that the absorptions for the outer annuli of $r > 5'$ were fixed at 2.4×10^{21} cm^{-2}, as described before. For fits of the inner three annuli, there are considerable deviations from the model below ~ 1.5 keV, which exhibits emission-line features indicating the presence of a cooler component. We then carried out double-temperature (2T) and triple-temperature (3T) model fits for the inner three annuli.

Downloaded from https://academic.oup.com/pasj/article/58/4/703/1456709 by Yildiz Teknik University Library (YTU) user on 25 February 2022

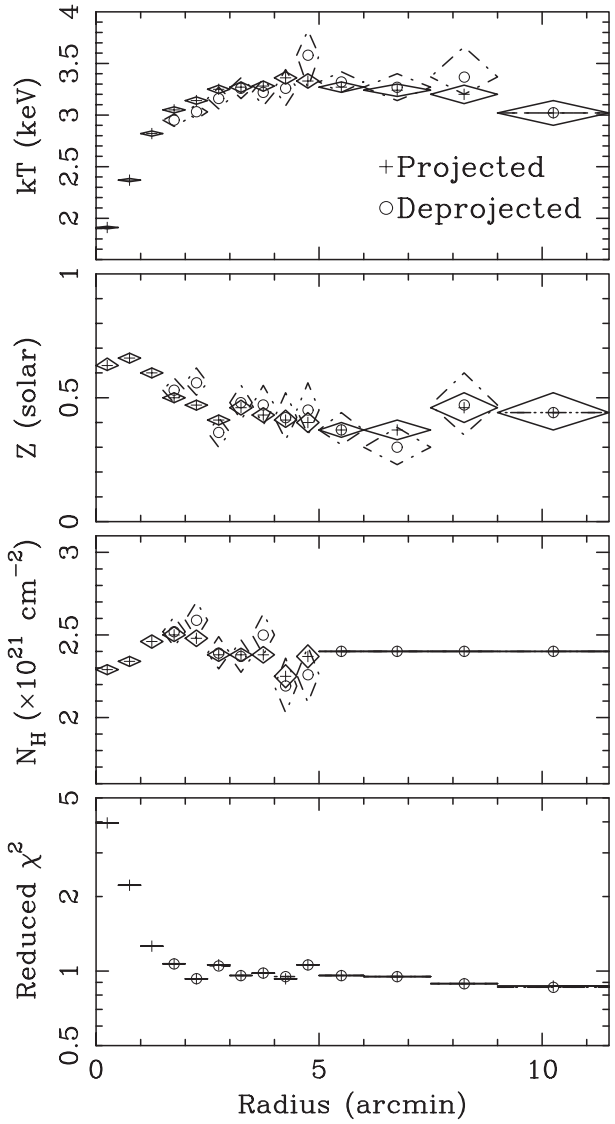


Fig. 4. Radial profiles of the temperature, metallicity, hydrogen column density, and reduced χ^2 of 2A 0335+096, obtained from single-temperature model fits to the 14 annular spectra within a radius of 11′.5. The cross and circle marks denote projected and deprojected profiles, respectively.

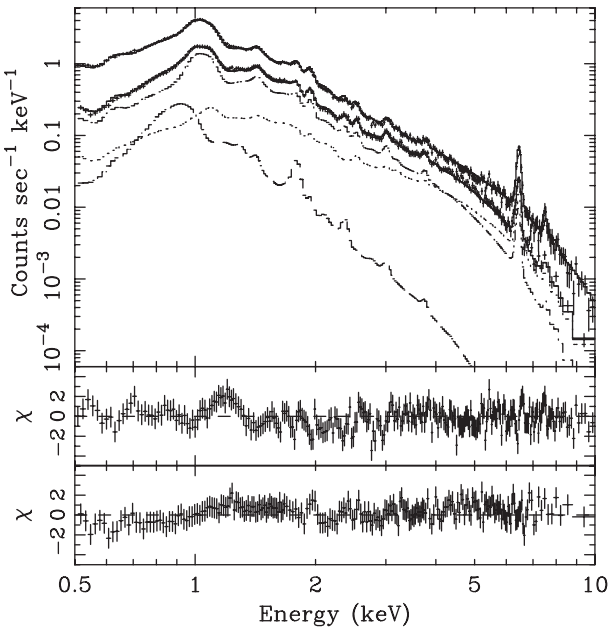


Fig. 5. MOS and pn spectra of $r = 0'$–$0'.5$ of 2A 0335+096. The uppermost spectrum denotes the pn spectrum, and the next denotes the MOS spectrum. These two spectra were simultaneously fitted with an absorbed triple-temperature model. The middle and bottom panels show the residual for the pn and MOS spectra, respectively. The best-fit models of the three components for the MOS spectrum are also plotted.

At first, an absorbed 2T model was employed. Since there is strong coupling between the metallicity and the normalization for a cool (kT = 1–2 keV) component, the metallicity of the cool component was linked to that of the other hot component. The results of the fits are summarized in table 2. The 2T model improved the fits markedly for the three annuli, and provided a satisfactory fit for the annuli of $r = 0'.5$–$1'$ and $r = 1'$–$1'.5$. For the two annuli, the two temperatures are 1.6–1.7 keV and 3.1–3.5 keV in common, the metallicity is 0.5–0.6 solar, and the hydrogen column density is (2.5–2.6) $\times 10^{21}$ cm^{-2}. As for the innermost region, still, an acceptable fit was not found. There were residuals around 1 keV, which indicate the presence of both cooler and hotter components than the best-fit temperature of $\sim$ 1.2 keV.

As a next step, we fitted with an absorbed 3T model. The metallicities of the three components were linked together. There was a remarkable improvement in the fits for the annuli of $r = 0'$–$0'.5$ and $r = 0'.5$–$1'$, to a statistically acceptable level. The best-fit parameters are listed in table 2, and the MOS and pn spectra with the best-fit absorbed 3T model for $r = 0'$–$0'.5$ are shown in figure 5. It turns out that the three temperatures are $\sim$ 0.8 keV, 1.6–1.7 keV, and $\sim$ 3.4 keV, in common for the inner two annuli. The steep positive gradient of the temperature in figure 4 shows that the two cooler components become dominant toward the center.

From the 2T and 3T model fits, the projected spectra of the inner three annuli were found to be well reproduced by the two or three temperature components. The derived temperatures are $\sim$ 0.8 keV, 1.6–1.7 keV, and 3.4–3.5 keV. The metallicity is 0.5–0.6 solar, and the hydrogen column density is (2.5–2.7) $\times 10^{21}$ cm^{-2}. Previous X-ray observations by Chandra have shown that the temperatures obtained by the 2T model fit for $r = 0''$–$250''$ are $\sim$ 1.4 keV and $\sim$ 3.3 keV (Mazzotta et al. 2003). Although the two temperatures are consistent with our results within the error, we presume that their lower value of 1.4 keV is attributed to the contribution of the $\sim$ 0.8 keV component. Here, it should be emphasized that the presence of the $\sim$ 0.8 keV and 1.6–1.7 keV components has been confirmed by the RGS analysis (see next section). As for the hydrogen column density, Mazzotta, Edge, and Markevitch (2003) have shown a lower absorption, which is consistent with the Galactic value. However, it should be noted that the XMM-Newton results by Kaastra et al. (2003) and Werner et al. (2006) and another Chandra result by Kawano et al. (2003) have shown an over-absorption of (2.6–2.9) $\times 10^{21}$ cm^{-2}, the same as our results.

Downloaded from https://academic.oup.com/pasj/article/58/4/703/1456709 by Yildiz Teknik University Library (YTU) user on 25 February 2022

Considering the projection effect, one might predict that the central temperature profile is merely due to a 3-dimensional (3D) radial distribution of the three components, namely, the ~ 0.8 keV component in the sphere of $r = 1'$, the 1.6–1.7 keV component in the shell of $r = 1'$–$1'.5$, and the 3.0–3.5 keV component outside $r = 1'.5$. In order to obtain the 3D radial profiles of the ICM, we subtracted the fore- and background emissions for the inner annuli. Here we adopted the deprojection method given by Blanton, Sarazin, and McNamara (2003), assuming a spherically symmetric distribution of the ICM. First, the spectrum from the outermost annulus was fitted with an absorbed 1T model; then, the inner next annulus was fitted with an absorbed 1T model along with the best-fit model of the exterior annulus with the normalization scaled to account for the spherical projection of the exterior shell onto the inner one. This process was continued inward as long as the fit was acceptable, fitting one spectrum with an absorbed 1T model at a time. The MOS spectrum extracted from $r = 11'.5$–$14'$ was used as the outermost annular spectrum. We also assumed that the temperature and metallicity of the ICM are constant beyond $r = 9'$ and are the same as the best-fit values of the absorbed 1T model for the spectrum of $r = 9'$–$11'.5$.

In the deprojection analysis, the absorbed 1T model was acceptable until an annulus of $r = 1'.5$–$2'$. The deprojected profiles are also shown in figure 4. We found no significant difference between the deprojected and projected profiles. Since the 1T model did not give an acceptable fit for an annulus of $r = 1'$–$1'.5$, we adopted the absorbed 2T model. The metallicities of the two components were linked together. The same as the projected case, the 2T model provided a good fit. Using the best-fit 2T model with the two normalizations scaled, we carried out a deprojection analysis on the next annulus of $r = 0'.5$–$1'$. Again, the same as in the projected case, we obtained a satisfactory fit with an absorbed 2T model and a better fit with an absorbed 3T model. We then used the best-fit 3T model for a deprojection analysis on the innermost annulus of $r = 0'$–$0'.5$, and obtained an acceptable fit with the absorbed 2T and 3T models. For the 3T model fit, the hottest temperature was fixed at 3.4 keV to examine the contribution of the surrounding hot gas. The results of the fits are summarized in table 3. Compared with the projected profiles (table 2), the temperatures of the 2T model fits for annuli of $r = 0'$–$0'.5$ and $r = 0'.5$–$1'$ are lower owing to the deprojection analysis. While the emission from the sphere of $r = 0'.5$ can be explained by ~ 0.9 keV and ~ 1.8 keV components, the shell region of $r = 1'$–$1'.5$ contains the ~ 1.7 keV and ~ 3.8 keV components. These results mean that the central gas in a sphere of $r = 1'.5$ consists of at least three components with different temperatures. The patchy temperature distribution of the central region by the Chandra observation (see figure 6 of Mazzotta et al. 2003) supports this idea.

3.3. RGS Results

As shown in figure 1, the X-ray brightness distribution exhibits a strong peak at the center, especially in the soft band. Thus, we expect relatively fine spectroscopy with the RGS for the central region. We extracted the first- and second-order spectra from the default region covering 90% for the fraction of the cross-dispersion PSF. For a spectral fit, we excluded the wavelength range where the estimated background was more than $\sim 25\%$ of the source flux. Since the cluster emission extends in the dispersion direction, we have to take into account the line broadening in the RGS analysis. Here, we utilized the rgsxsrc model implemented in XSPEC v11.3, which convolves a spectral model with an angular structure function. The EPIC MOS image was used as the angular structure function.

As stated by Werner et al. (2006), the Fe-L complex, including the Ne-K line and the K-lines of O, Mg, Si, were detected in the RGS spectra. For the Fe-L complex, we identified the lines from the ionization states ranging from Fe XVII to Fe XXIV. As the first attempt, we fitted the first- and second-order spectra simultaneously with an absorbed 1T model. However, we did not find an acceptable fit with this 1T model. This is consistent with the result of Werner et al. (2006).

Table 2. Best-fit parameters.*

Annulus	$0'$–$0'.5$		$0'.5$–$1'$		$1'$–$1'.5$
Model	2T	3T	2T	3T	2T
kT_1 (keV)	$2.34^{+0.07}_{-0.06}$	$3.43^{+0.26}_{-0.31}$	$3.09^{+0.21}_{-0.15}$	$3.43^{+0.26}_{-0.24}$	$3.47^{+0.24}_{-0.13}$
kT_2 (keV)	$1.23^{+0.03}_{-0.04}$	$1.64^{+0.04}_{-0.04}$	$1.59^{+0.05}_{-0.06}$	$1.72^{+0.14}_{-0.05}$	$1.72^{+0.20}_{-0.04}$
kT_3 (keV)	⋯	$0.81^{+0.03}_{-0.04}$	⋯	$0.80^{+0.07}_{-0.13}$	⋯
Norm_1 $(10^{-3})^\dagger$	$8.75^{+0.48}_{-0.50}$	$2.98^{+0.76}_{-0.44}$	$10.53^{+1.30}_{-1.39}$	$7.98^{+1.42}_{-1.71}$	$8.42^{+0.65}_{-1.42}$
Norm_2 $(10^{-3})^\dagger$	$3.74^{+0.65}_{-0.61}$	$8.95^{+0.43}_{-0.74}$	$7.95^{+1.55}_{-1.43}$	$10.07^{+1.64}_{-1.41}$	$4.09^{+1.45}_{-0.71}$
Norm_3 $(10^{-3})^\dagger$	⋯	$0.83^{+0.11}_{-0.11}$	⋯	$0.40^{+0.09}_{-0.15}$	⋯
Z (solar)	$0.62^{+0.03}_{-0.03}$	$0.62^{+0.03}_{-0.03}$	$0.56^{+0.02}_{-0.02}$	$0.59^{+0.02}_{-0.02}$	$0.53^{+0.02}_{-0.02}$
N_H $(10^{21}\,\mathrm{cm}^{-2})$	$2.42^{+0.03}_{-0.03}$	$2.56^{+0.04}_{-0.04}$	$2.59^{+0.04}_{-0.04}$	$2.67^{+0.05}_{-0.05}$	$2.54^{+0.04}_{-0.04}$
χ^2_ν (d.o.f.)	1.30 (494)	1.02 (492)	0.95 (486)	0.87 (484)	0.83 (486)

* Best-fit parameters of absorbed double- and triple-temperature models for the inner three annular regions of 2A 0335+096, with reference to the projection.

† The normalization of the APEC model, implemented in XSPEC, is defined as $10^{-14}/[4\pi D_\mathrm{A}^2(1+z)^2]\int n_\mathrm{e} n_\mathrm{H}\, dV$, where n_e and n_H are the electron and hydrogen densities in cm^{-3}, respectively, and D_A is the angular size distance in cm.

Downloaded from https://academic.oup.com/pasj/article/58/4/703/1456709 by Yildiz Teknik University Library (YTU) user on 25 February 2022

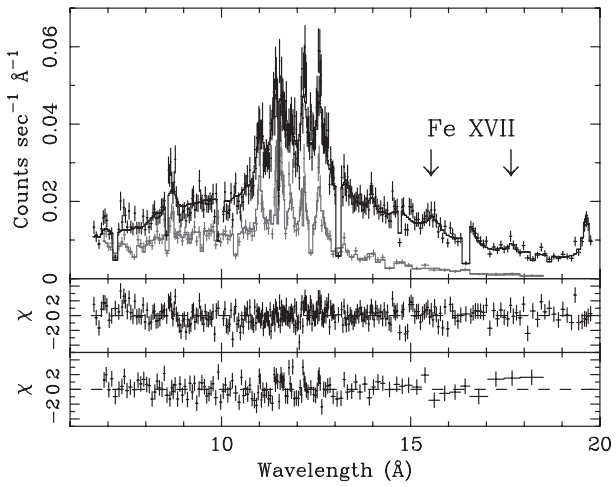


Fig. 6. RGS spectra of the central region of 2A 0335 + 096. The upper spectrum denotes the RGS2 first-order spectrum, and the lower denotes the RGS1 second-order spectrum. These two spectra were simultaneously fitted with an absorbed double-temperature model. The middle and bottom panels show the residual for RGS2 and RGS1 spectra, respectively.

We then employed an absorbed 2T model. The metallicities of the two components were linked together in accordance with the EPIC spectral analysis. The results of the fits are shown in figure 6 and summarized in table 4. The 2T model improved the fits markedly. One can see that the 2T model reproduces the overall spectral structure fairly well. Allowing individual elemental abundances to vary did not significantly improve the fits. The obtained two temperatures are 0.7–0.8 keV and 1.7–1.8 keV, which are in agreement with the EPIC results. Since the Fe XVII lines, the positions of which are denoted in figure 6, become prominent in the temperature range of 0.2–0.8 keV, the presence of the 0.7–0.8 keV component would be reliable. The hydrogen column density is not consistent with the results of RGS1 and RGS2, although the lower value of RGS2 is in agreement with that of the EPIC results. It is worth noting that an absorbed 3T model did not significantly improve the fits.

Table 4. Best-fit parameters of an absorbed double-temperature model for the RGS1 and RGS2 spectra.

Parameter	RGS1	RGS2
kT_1 (keV)	$0.73^{+0.07}_{-0.05}$	$0.79^{+0.02}_{-0.03}$
kT_2 (keV)	$1.72^{+0.04}_{-0.12}$	$1.79^{+0.09}_{-0.08}$
Z (solar)	$0.46^{+0.05}_{-0.07}$	$0.45^{+0.06}_{-0.06}$
$N_{\rm H}$ (10^{21} cm^{-2})	$3.10^{+0.10}_{-0.09}$	$2.70^{+0.11}_{-0.11}$
χ^2_ν (d.o.f.)	1.22 (331)	1.26 (413)

Table 5. Best-fit parameters.*

Region	kT (keV)	Z (solar)	χ^2_ν (d.o.f.)
NE	$3.18^{+0.10}_{-0.10}$	$0.44^{+0.07}_{-0.07}$	1.02 (249)
NW	$3.37^{+0.12}_{-0.09}$	$0.42^{+0.06}_{-0.06}$	0.99 (249)
SE	$2.95^{+0.09}_{-0.09}$	$0.44^{+0.06}_{-0.06}$	0.91 (249)
SW	$3.61^{+0.16}_{-0.16}$	$0.46^{+0.09}_{-0.08}$	1.05 (249)

* Best-fit parameters of an absorbed single-temperature model in the energy region 1–10 keV. The four regions are shown on the *SR* map of I(1–2 keV)/I(2–10 keV) of 2A 0335 + 096 (figure 7).

3.4. 2D Temperature Profiles

By making a softness ratio (SR) map from the EPIC data, we investigated the 2D temperature distribution. In order to study the distribution for the outer region, we first made a low-resolution *SR* map with a pixel size of 32.″8. The *SR* is defined as the 1–2 keV intensity divided by the 2–10 keV intensity. The soft energy band below $\sim$ 1 keV is not used because it would be affected by soft X-rays from the local environment and the photoelectric absorption by our galaxy's interstellar medium, especially for the outer low-brightness region. The combined MOS and pn images in the energy 1–2 keV and 2–10 keV are binned to pixels of 32.″8, filtered with a σ = 32.″8 Gaussian and divided.

Table 3. Same as table 2, but with reference to the deprojection.

Annulus	0′–0.′5		0.′5–1′		1′–1.′5
Model	2T	3T	2T	3T	2T
kT_1 (keV)	$1.78^{+0.04}_{-0.04}$	3.40*	$2.39^{+0.09}_{-0.07}$	$3.41^{+0.65}_{-0.52}$	$3.81^{+0.50}_{-0.32}$
kT_2 (keV)	$0.94^{+0.04}_{-0.06}$	$1.59^{+0.05}_{-0.06}$	$1.28^{+0.05}_{-0.10}$	$1.75^{+0.15}_{-0.11}$	$1.70^{+0.13}_{-0.05}$
kT_3 (keV)	···	$0.81^{+0.04}_{-0.04}$	···	$0.80^{+0.06}_{-0.12}$	···
Norm$_1$ (10^{-3})	$5.45^{+0.22}_{-0.22}$	$0.54^{+0.19}_{-0.18}$	$9.42^{+0.57}_{-0.60}$	$3.40^{+1.88}_{-1.45}$	$3.54^{+0.55}_{-0.79}$
Norm$_2$ (10^{-3})	$1.02^{+0.21}_{-0.19}$	$5.63^{+0.30}_{-0.29}$	$2.03^{+0.75}_{-0.68}$	$7.91^{+1.37}_{-1.90}$	$3.30^{+0.85}_{-0.64}$
Norm$_3$ (10^{-3})	···	$0.66^{+0.10}_{-0.10}$	···	$0.39^{+0.08}_{-0.14}$	···
Z (solar)	$0.71^{+0.06}_{-0.06}$	$0.64^{+0.06}_{-0.06}$	$0.64^{+0.05}_{-0.05}$	$0.63^{+0.04}_{-0.04}$	$0.56^{+0.05}_{-0.04}$
$N_{\rm H}$ (10^{21} cm^{-2})	$2.40^{+0.06}_{-0.06}$	$2.49^{+0.08}_{-0.08}$	$2.62^{+0.07}_{-0.07}$	$2.73^{+0.08}_{-0.08}$	$2.56^{+0.08}_{-0.08}$
χ^2_ν (d.o.f.)	1.06 (494)	1.03 (493)	0.93 (486)	0.86 (484)	0.84 (486)

* The temperature is fixed at 3.4 keV of the ambient hot gas.

Downloaded from https://academic.oup.com/pasj/article/58/4/703/1456709 by Yildiz Teknik University Library (YTU) user on 25 February 2022

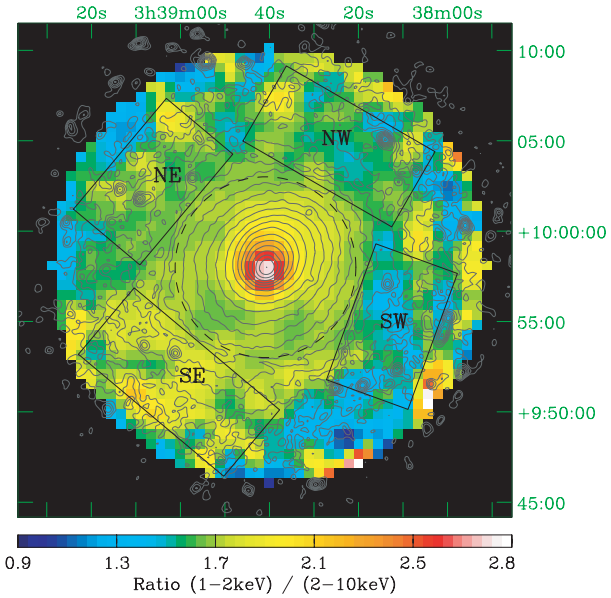


Fig. 7. *SR* map of I(1–2 keV)/I(2–10 keV) within a radius of 12′ of 2A 0335+096. The gray contours are the same as those in figure 1. The central circle of $r = 5'$ refers to the zoomed-in *SR* map shown in figure 8. The labeled boxes identify the regions for spectral analysis.

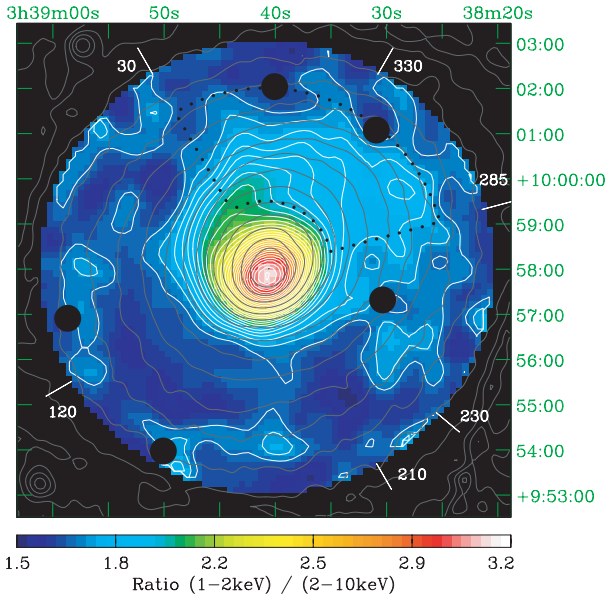


Fig. 8. *SR* map of I(1–2 keV)/I(2–10 keV) within a radius of 5′ of 2A 0335+096. The gray contours are the same as those in figure 1. Point sources are masked out. Short lines outside the map mark a sector used to show the significance of the softness gradient (figure 9). The sector delineated by a dotted line shows an extraction region for the spectral analysis of the soft tail.

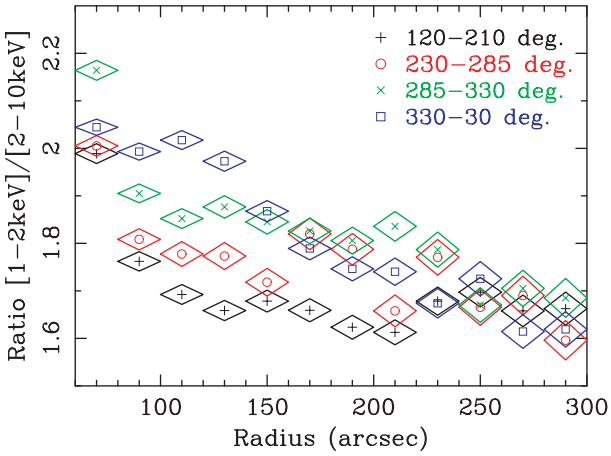


Fig. 9. Radial profiles of the softness ratio for the sectors in $r = 1'$–5′. The position angles (north to east) of the sectors are 120°–210°, 230°–285°, 285°–330°, and 330°–30°. The errors are 1σ.

Figure 7 shows the *SR* map of 2A 0335+096 within a radius of 12′. The map exhibits the softest region at the X-ray peak, where the two or three temperature components have been found through EPIC and RGS spectral analyses. One can see that the central soft region is extended in northwesterly and westerly directions. This feature is consistent with the elongated temperature structure seen in Werner et al. (2006). One can also find that the *SR* distribution for the outer region of $r > 5'$ is not azimuthally symmetric. A soft region is easily identified in the southeast, while a hard region is apparent in the southwest. It seems that the spectrum of the outer region becomes harder clockwise from the southeast to the southwest. To verify the statistical significance of this structure, we extracted spectra from the four box regions shown on the *SR* map (labeled "NE", "NW", "SE", and "SW") and performed spectral fits in the energy region 1–10 keV with an absorbed 1T model. The absorption was fixed at 2.4×10^{21} cm^{-2} in the same way as in the spectral analysis for the outer annular regions. The best-fit values are listed in table 5. We found a clockwise temperature increase in accordance with the *SR* profile, from the region "SE" of 3 keV to the region "SW" of 3.6 keV.

We then produced a high-resolution *SR* map within a radius of 5′ to study the detailed temperature distribution. The central broken circle in figure 7 delineates the selected region. Figure 8 shows a high-resolution *SR* map. The pixel size of the map is 8.″2 and a σ = 16.″4 Gaussian was used as the smoothing function. To accentuate the *SR* structure, white contour lines are overlaid on the map. One can see from the map that the central cold core is trailing the spiral soft tail, which arises on the opposite side of the cold front. To see the significance of the tail structure, we examined the radial profiles of the *SR* for four sectors, the position angles (*PA*) of which are 120°–210°, 230°–285°, 285°–330°, and 330°–30°, as marked outside the *SR* map. The sector *PA* = 120°–210° is referential. The profiles with 1σ error are shown in figure 9. The radial bin width is 20″. The radial profile of the *PA* = 120°–210° sector shows uniformity beyond r = 100″. Compared with the referential sector, we detected a 3–4σ excess on average at r = 160″–240″ in the sector *PA* = 230°–285°, which corresponds to the end of the soft tail. For both sectors *PA* = 285°–330° and *PA* = 330°–30°, a significant excess of more than 5σ was demonstrated.

In order to confirm a temperature difference between the soft tail and referential regions, we extracted spectra from the sectors *PA* = 120°–210° and 285°–30° in r = 1.′5–11.′5, and fitted with an absorbed 1T model. The temperature profiles are

Downloaded from https://academic.oup.com/pasj/article/58/4/703/1456709 by Yildiz Teknik University Library (YTU) user on 25 February 2022

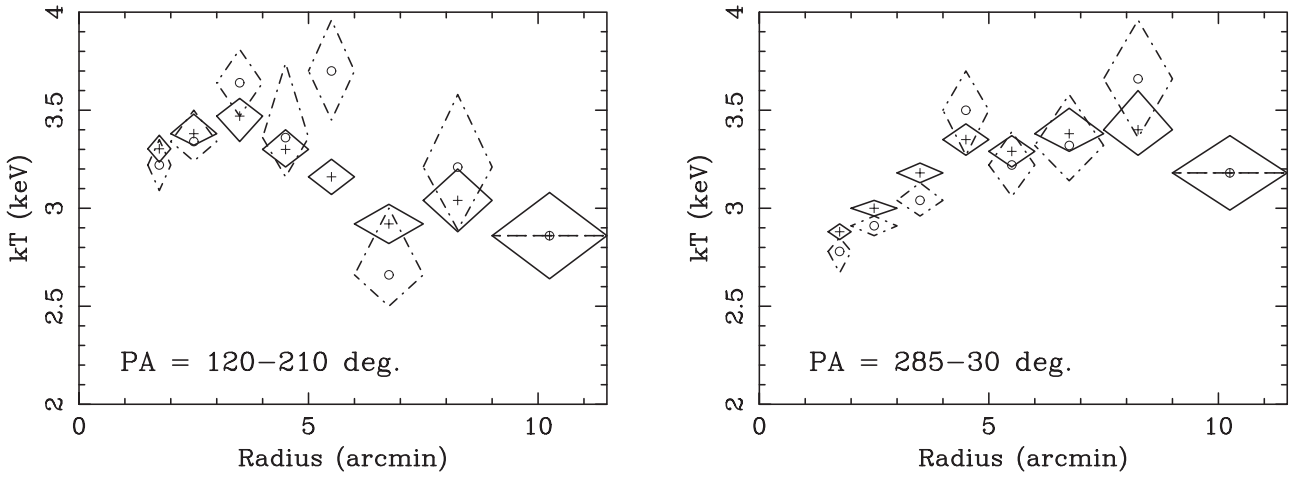


Fig. 10. Radial temperature profiles of 2A 0335+096 for position angles 120°–210° (left) and 285°–30° (right), obtained from single-temperature fits. The cross and circle marks denote the projected and deprojected profiles, respectively.

shown in figure 10. The absorbed 1T model gives an acceptable fit for all spectra. In accordance with the *SR* map, the temperature profile for $PA = 120°$–$210°$ shows a modest temperature decline beyond $r = 5'$, from 3.3–3.5 keV at the inner regions to 2.9–3 keV at outer regions, and for $PA = 285°$–$30°$ we see a temperature decrease within $r = 4'$, from 3.3–3.4 keV down to 2.9 keV at the innermost sector. We also performed a deprojection analysis in the same manner as was done for the annular spectra. The profiles are also shown in figure 10. We confirmed the significant differences for the three sectors in $r = 1.'5$–$4'$, where the temperatures are 3.2–3.6 keV for $PA = 120°$–$210°$ and 2.8–3.0 keV for $PA = 285°$–$30°$.

3.5. Spectrum of the Soft Tail

In order to determine the spectrum of the soft tail, we had to remove the fore- and background emissions from the ambient cluster gas along the line of sight. Assuming that the soft tail does not extend in any direction beyond its outermost projected radius of $4'$, thus by adopting the deprojection analysis described before, we could obtain a spectrum consisting of the tail emission and the ambient emission from the shell region $r = 1.'5$–$4'$.

We performed a deprojection analysis on the spectra from the sector $PA = 285°$–$30°$ in $r = 1.'5$–$4'$, which is delineated by a dotted line in figure 8. After deprojection, we fitted with two simple models. First, we used an absorbed 1T model, which necessarily assumes that the volume filling factor is 1 as long as the model is acceptable. Second, we fitted with an absorbed 2T model to take into account the emission from the ambient gas near the tail. The temperature and metallicity of the ambient gas were assumed to be 3.4 keV and 0.45 solar, respectively, based on the results of the referential region $PA = 120°$–$210°$. The results of the spectral fits are summarized in table 6. We found a satisfactory fit with both models, and a much better fit with the absorbed 2T model. The MOS and pn spectra with the best-fit absorbed 2T model are shown in figure 11. It should be noted that the temperature of 1.7 keV obtained by the 2T model is consistent with one of the three temperatures obtained for the central region of $r < 1.'5$.

4. Abell 496

4.1. X-Ray Morphology

Figure 12 shows the MOS contour map overlaid on the DSS optical image for A 496. The image was created in the same manner as was done for 2A 0335+096. Compared to 2A 0335+096, the X-ray brightness distribution of A 496 is fairly elongated in north-northwesterly and south-southeasterly directions. It is apparent that the X-ray emission peak coincides with the cD galaxy, MCG-02-12-039. One can easily identify the sharp edge in the surface brightness $\sim 1.'5$ north of the cD galaxy, which was studied by Dupke and White (2003) using the Chandra data. Furthermore, we found that there is a fairly sharp brightness edge at $r \sim 4'$ south of the cD galaxy. We note that the brightness feature of two sharp edges on opposite sides of the X-ray peak is quite similar to that found for RX J1720.1+2638 (Mazzotta et al. 2001).

The surface brightness profiles in the energy ranges

Table 6. Best-fit parameters.*

Model	kT_1 (keV)	kT_2 (keV)	Z_1 (solar)	Z_2 (solar)	N_H (10^{21} cm^{-2})	χ^2_ν (d.o.f.)
1T	$2.96^{+0.03}_{-0.03}$	···	$0.48^{+0.02}_{-0.02}$	···	$2.42^{+0.04}_{-0.04}$	1.02 (447)
2T	3.4†	$1.70^{+0.15}_{-0.06}$	0.45*	$0.48^{+0.13}_{-0.10}$	$2.46^{+0.05}_{-0.05}$	0.83 (446)

* Best-fit parameters of absorbed single- and double-temperature fits to the spectra from the sector region of $PA = 285°$–$30°$ in $r = 1.'5$–$4'$, which is delineated by a dotted line in figure 8.

† The temperature and metallicity of the ambient gas are assumed to be 3.4 keV and 0.45 solar, respectively.

Downloaded from https://academic.oup.com/pasj/article/58/4/703/1456709 by Yildiz Teknik University Library (YTU) user on 25 February 2022

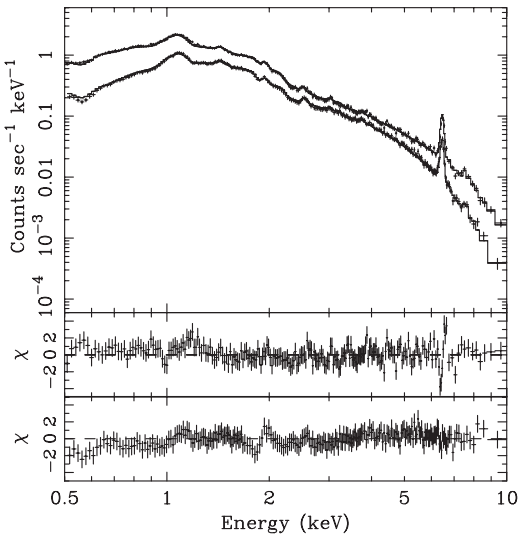


Fig. 11. MOS and pn spectra of the sector region $PA = 285°$–$30°$ in $r = 1.'5$–$4'$, which is delineated by a dotted line in figure 8. The upper spectrum denotes the pn spectrum, and the lower denotes the MOS spectrum. These two spectra were simultaneously fitted with an absorbed double-temperature model after the deprojection analysis.

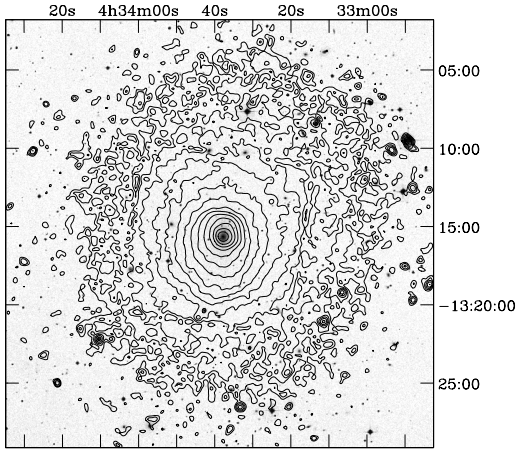


Fig. 12. Same as figure 1, but with reference to A 496.

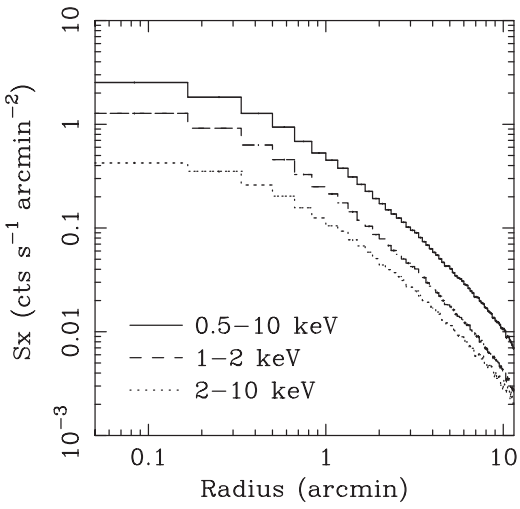


Fig. 13. Same as figure 2, but with reference to A 496.

0.5–10 keV, 1–2 keV, and 2–10 keV are shown in figure 13. Similarly in the case 2A 0335+096, the 1–2 keV profile exhibits a more centrally concentrated brightness distribution than the 2–10 keV profile.

Figure 14 shows a map of the relative deviation from the azimuthally averaged value, made in the same manner as was done for 2A 0335+096. As can be seen in the X-ray contours, the sharp brightness edges $\sim 1.'5$ north and $\sim 4'$ south of the X-ray peak are accentuated in the map. For the outside region, we can see fairly-asymmetric structures, namely, a stronger excess north-northwest than south-southeast, and a depression east compared with the west side. The outside asymmetric structure indicates that the X-ray peak is displaced from the center of the cluster, determined on a large scale.

4.2. Radial Profiles

Following the same procedures as were done for 2A 0335+096, we studied the radial profiles of the temperature and metallicity. First, we obtained the projected profiles by fitting the annular spectra with an absorbed 1T model. The results of the fits are shown in figure 15. We confirmed that the temperature increases with the radius from 2.5 keV at the central region up to ~ 5 keV for $r > 4'$, while the metallicity decreases outward from 0.8 solar to 0.3–0.4 solar. The hydrogen column density is marginally consistent with the Galactic value of $(0.4–0.5) \times 10^{21}$ cm^{-2}, obtained from the 21 cm measurement (Dickey, Lockman 1990). The absorbed 1T model gives acceptable fits for the outer 13 annuli, but a tentative fit for the innermost region. For the spectrum of the innermost region, we see excess line features in the residual below ~ 1.5 keV, indicating the presence of a cooler component.

As a next attempt, we investigated the deprojected profiles using the same deprojection method as was done for 2A 0335+096. The results are also shown in figure 15. We found a considerable improvement of the fit for the innermost region to an acceptable level. Therefore, an additional component is not necessary for A 496. Compared with the projected profile, the temperature profile shows a systematic temperature drop for the inner three annuli, which is attributed to removal of the outer hot-gas emission in the deprojection analysis. We confirmed that the projected and deprojected profiles are consistent with the previous XMM-Newton results by Tamura et al. (2001b).

4.3. 2D Temperature Profiles

Figure 16 shows an *SR* map of $I(1–2\,\mathrm{keV})/I(2–10\,\mathrm{keV})$ for A 496. It is apparent that the *SR* distribution is not uniform. We can see the softest region at the X-ray brightness peak and remarkable asymmetric variations on the whole. The overall variations suggest that this cluster is not relaxed. Thus, the radial temperature increase (figure 15), typically seen in a relaxed cluster, is presumed to be the result of averaging over annuli with azimuthal temperature variations. For the outside region of $r > 5'$ between the north and the west, we found a patchy softness distribution, which seems to be related to the brightness residuals seen in figure 14. For the central region, we can see a steep softness gradient across both the northern and southern edges, inside of which the emission is softer.

Downloaded from https://academic.oup.com/pasj/article/58/4/703/1456709 by Yildiz Teknik University Library (YTU) user on 25 February 2022

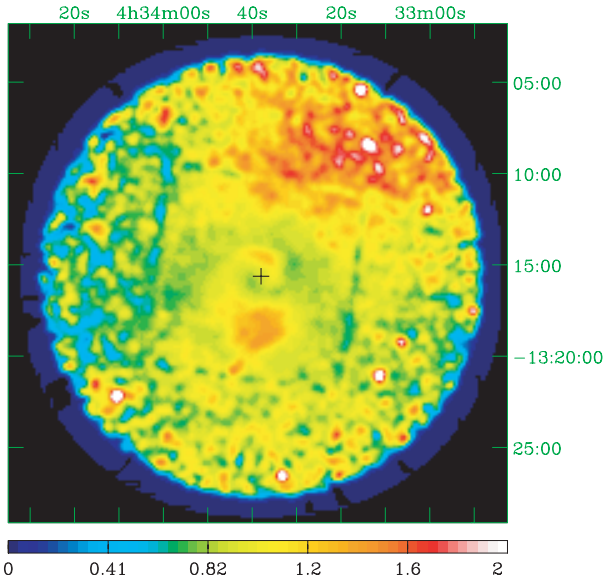


Fig. 14. Same as figure 3, but with reference to A 496.

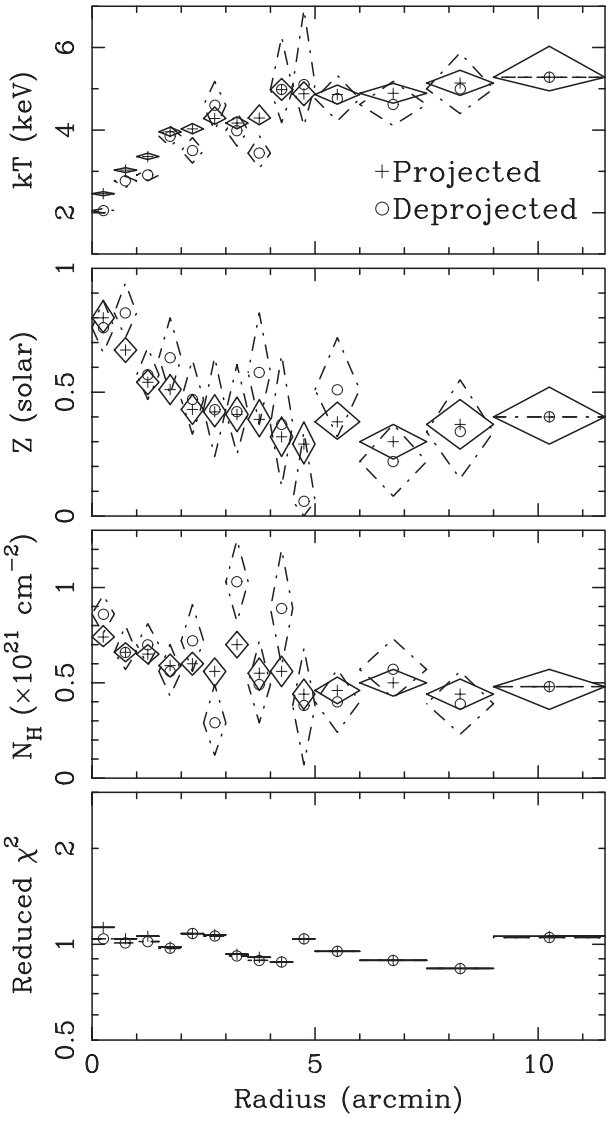


Fig. 15. Same as figure 4, but with reference to A 496.

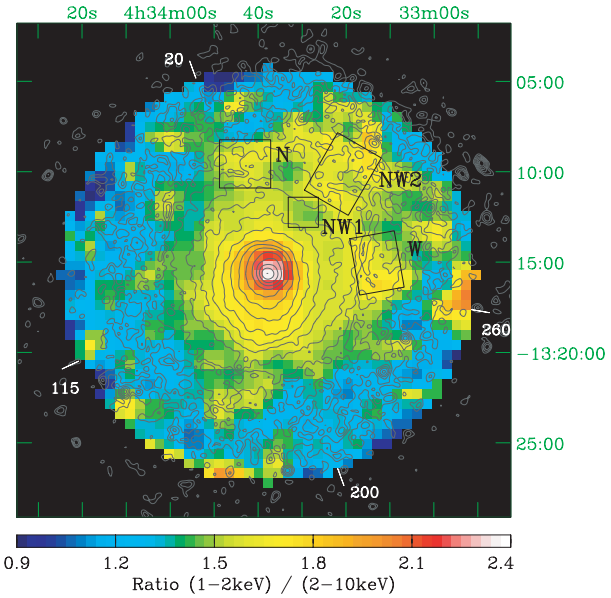


Fig. 16. Same as figure 7, but with reference to A 496. The short lines outside the map mark the sectors used for the radial spectral analysis. The labeled boxes identify the extraction regions for spectral analysis.

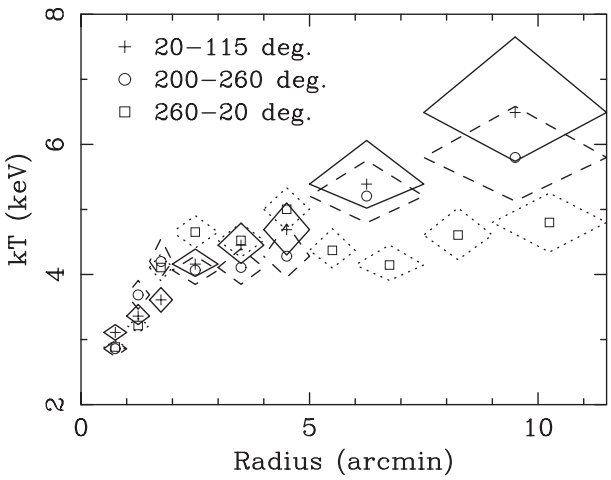


Fig. 17. Radial temperature profiles of A 496 for *PA* = 20°–115° (cross), 200°–260° (circle), and 260°–20° (box).

We recall that the gas profiles across the northern edge are consistent with the characteristics of the cold front (Dupke, White 2003). Here we emphasize that those *SR* structures are located along the elongation of the X-ray brightness distribution.

To confirm the non-uniform temperature structures on the overall region, we extracted spectra from the sector regions *PA* = 20°–115°, 200°–260°, and 260°–20°, as denoted by the short lines outside the *SR* map (figure 16), and then fitted with an absorbed 1T model. The gas profiles across the southern edge in the sector *PA* = 115°–200° is presented in the following section. The temperature profiles of the sector regions are shown in figure 17. Whereas the temperature distributions for *PA* = 20°–115° and 200°–260° show a similar increase with

Downloaded from https://academic.oup.com/pasj/article/58/4/703/1456709 by Yildiz Teknik University Library (YTU) user on 25 February 2022

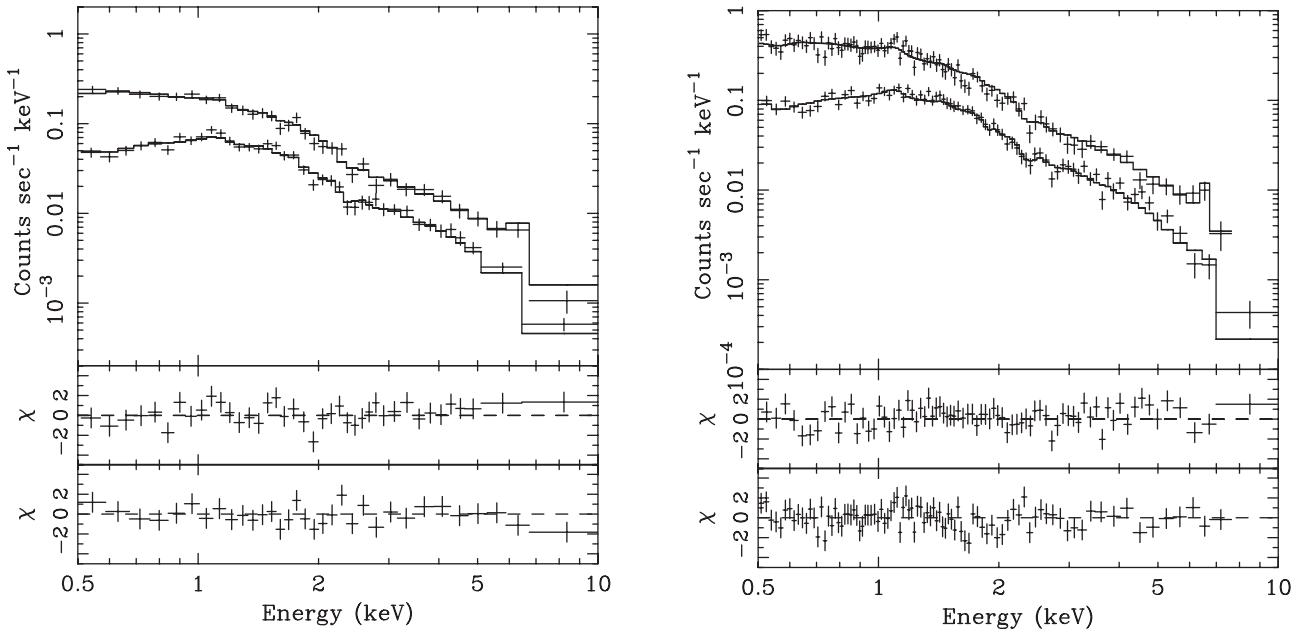


Fig. 18. MOS and pn spectra of regions "NW1" (left) and "NW2" (right), shown in the *SR* map of $I(1\text{–}2\,\mathrm{keV})/I(2\text{–}10\,\mathrm{keV})$ (figure 16). The upper and lower spectra in the top panel denote the pn and MOS spectra, respectively. The middle and bottom panels show the residual for the pn and MOS spectra, respectively.

Table 7. Best-fit parameters.*

Region	kT (keV)	Z (solar)	N_{H} ($10^{21}\,\mathrm{cm}^{-2}$)	χ^2_ν (d.o.f.)
NW1	$5.51^{+0.74}_{-0.49}$	$0.56^{+0.28}_{-0.26}$	$0.32^{+0.14}_{-0.14}$	0.92 (69)
NW2	$4.12^{+0.34}_{-0.28}$	$0.34^{+0.12}_{-0.12}$	$0.41^{+0.12}_{-0.11}$	1.09 (167)
N	$4.20^{+0.56}_{-0.35}$	$0.53^{+0.24}_{-0.21}$	$0.56^{+0.15}_{-0.16}$	1.33 (67)
W	$3.79^{+0.37}_{-0.36}$	$0.32^{+0.18}_{-0.16}$	$0.60^{+0.16}_{-0.16}$	1.01 (67)

* Best-fit parameters of an absorbed single-temperature model for the four box regions shown on the *SR* map of $I(1\text{–}2\,\mathrm{keV})/I(2\text{–}10\,\mathrm{keV})$ of A 496 (figure 16).

the radius, the temperature profile for $PA = 260°$–$20°$ exhibits a modest drop to 4–4.5 keV at $r = 5'$–$9'$.

To see the statistical significance of the patchy *SR* structures at $r > 5'$ between the north and the west, we extracted spectra from the four box regions shown in figure 16, labeled "N", "NW1", "NW2", and "W", and fitted with an absorbed 1T model. Figure 18 shows spectral-fit examples for regions "NW1" and "NW2". The best-fit parameters are summarized in table 7. It is apparent that there is a significant difference for the temperature between the high-*SR* region 3.8–4.2 keV and the low-*SR* region at 5.5 keV.

4.4. Gas Profiles across the Edge

In order to study the gas profiles across the southern brightness edge, we extracted the surface brightness and spectra from the sector $PA = 115°$–$200°$. The 0.5–2 keV surface brightness distribution in the sector is plotted in panel (a) of figure 19. The energy band was chosen to minimize the dependence of the X-ray emissivity on the temperature and to maximize the signal-to-noise ratio. A sharp brightness edge can be seen at $r \sim 4'$. Since the brightness distribution has a similar profile to that found in other clusters with cold fronts, one can expect the presence of a gas density discontinuity. Referring to the density model shown in Markevitch et al. (2000), we fitted the brightness profile with a radial density model of two power laws separated by a jump under the assumption of a spherically symmetric distribution. The fitting range is $r = 2'$–$11'$. We found that the density model can well reproduce the overall brightness profile with $\chi^2_\nu(\mathrm{d.o.f.}) = 0.83\,(31)$. The brightness profile derived from the density model is overlaid in panel (a). The vertical dotted line shows the position of the density jump, $r = 4\farcm0 \pm 0\farcm1$. The obtained power-law indexes for inside and outside of the jump are -0.94 ± 0.08 and -1.53 ± 0.03, respectively. We then derived the temperature profile across the edge from wider sector regions so that the spectrum would include sufficient counts. Panel (b) of figure 19 shows both projected and deprojected temperature profiles. One can see a temperature jump across the density jump, ~ 4 keV inside to ~ 5 keV outside. Panel (c) of figure 19 shows the electron density distribution along with the power-law density model. The density was derived from the APEC normalization, defined as $K = 10^{-14}/[4\pi D_{\mathrm{A}}^2(1+z)^2]\int n_{\mathrm{e}} n_{\mathrm{H}}\, dV$, where n_{e} and n_{H} are the electron and hydrogen densities in cm^{-3}, respectively, and D_{A} is the angular size distance to the source in cm. The factor

Downloaded from https://academic.oup.com/pasj/article/58/4/703/1456709 by Yildiz Teknik University Library (YTU) user on 25 February 2022

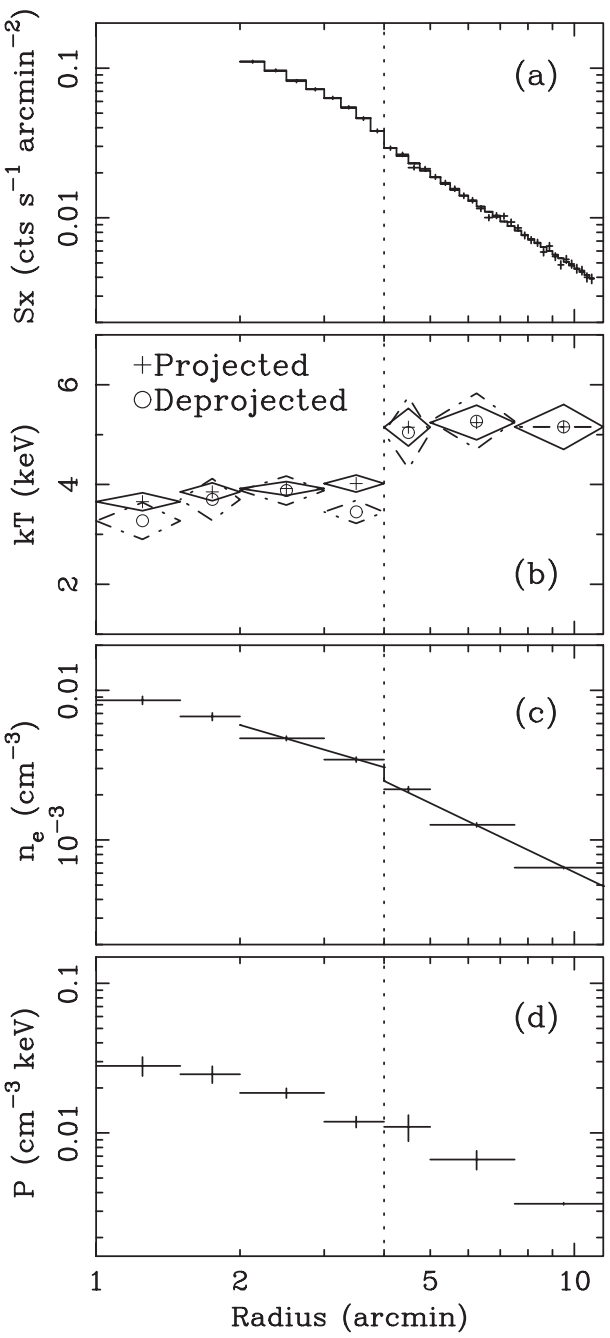


Fig. 19. Profiles of the southern sector $PA = 115°$–$200°$. The vertical dotted line denotes the edge position. (a) Surface brightness in the energy range 0.5–2 keV. The errors are 1σ. (b) Projected and deprojected temperature profiles. (c) Profile of the electron density along with the density model. (d) Pressure profile.

of the density jump at the discontinuous position is 1.27 ± 0.11, which is relatively low among the clusters with cold fronts. The pressure profile obtained by multiplying the measured temperature value and the electron density is shown in panel (d) of figure 19. Since the jump factors of the gas density and temperature cancel out each other, the pressure across the edge is continuous. These features are consistent with the characteristics of a cold front.

5. Discussion

We analyzed the XMM-Newton data of the galaxy clusters 2A 0335+096 and A 496. Taking advantage of the XMM-Newton's wide field of view, moderate angular resolution, and large collecting area, we found interesting gas profiles in both clusters. For 2A 0335+096, we detected a cool tail feature emerging northwest of the central cold dense core and an asymmetric temperature distribution in the outer region. For A 496, we found another cold front $4'$ south of the X-ray emission peak and cool regions at $r \sim 5'$–$9'$ in the north and west directions. Below, we discuss possible interpretations of these results.

5.1. Cool Tail of 2A 0335+096

The X-ray surface brightness extension toward the northwest in the central region and the presence of a cold front observed by Chandra (Mazzotta et al. 2003) suggest that the core came from the northwest and changed its direction to the south. An investigation of the 2D temperature distribution revealed a cool tail feature, which coincides with the extended brightness feature. It is thus reasonable to suppose that the cool tail is related to the non-linear motion of the central core. Here, we discuss three possible mechanisms for the formation of the cool tail, the cooling wake (David et al. 1994; Fabian et al. 2001), the ram-pressure stripping (e.g., Gunn, Gott 1972), and the turbulent viscous stripping due to the Kelvin–Helmholtz instability (e.g., Nulsen 1982).

The cooling wake is produced by a cooling flow occurring around a moving body. Some overdense clumps in the cooling flow are gravitationally focused into a wake along the path of a moving body, and produce a cool trail feature (David et al. 1994; Fabian et al. 2001). In order to check if the cooling flow occurs at the tail region, we derived the cooling time of the gas around the tail. The average electron density of the gas was obtained by using normalization of the absorbed 1T model used in the fits for the spectrum of the sector region (see table 6). Adopting the derived electron density of $\sim 5 \times 10^{-3}$ and the ambient gas temperature of 3.4 keV, we estimated that the cooling time is $\sim 1 \times 10^{10}$ yr. Since the cooling time is comparable to the Hubble time, it is unlikely that the cooling wake is responsible for forming of the cool tail.

As for ram-pressure stripping, the gas of the cold core is partly pushed out by the ram pressure caused by the core's motion through the ICM when the ram pressure exceeds the gravitational force holding the gas in the core. Thus, the cool tail trailing behind the core may be due to the stripped gas. Here, we recall a discussion concerning the Rayleigh–Taylor instability stated in Mazzotta, Edge, and Markevitch (2003). They compared the acceleration induced by the drag force with the gravitational acceleration to see if the Rayleigh–Taylor instability can explain the origin of the complex structure in the core. Since the ram pressure is exerted on a moving body by the drag force, their comparison can be applied to our discussion on the possibility of ram-pressure stripping. According to Mazzotta, Edge, and Markevitch (2003), the acceleration induced by the drag force and the gravitational acceleration are $2.5 \times 10^{-9}\,\mathrm{cm\,s^{-2}}$ and $1.7 \times 10^{-8}\,\mathrm{cm\,s^{-2}}$, respectively. This result means that the ram-pressure stripping does not seem to

Downloaded from https://academic.oup.com/pasj/article/58/4/703/1456709 by Yildiz Teknik University Library (YTU) user on 25 February 2022

occur for the core.

Another stripping process that we propose is turbulent viscous stripping due to the Kelvin–Helmholtz instability, where gas is removed when momentum is transferred to the core gas by the action of turbulence and viscosity at the interface between the core and ICM during this motion (e.g., Nulsen 1982). The Kelvin–Helmholtz instability has also been discussed by Mazzotta, Edge, and Markevitch (2003) as a process responsible for the formation of the complex structure in the core. They have shown that the gravitational acceleration at the interface suppresses instabilities only on scales larger than 400 kpc, which is much larger than the scale of the core; also, the growth time of the instability is much shorter than the dynamical time of the system, so that the formation of the Kelvin–Helmholtz instability is expected. As a result of the instability growth, some ambient hot gas would be deposited into the cold core, and some dense cool gas would be removed from the core. The mixing process has been suggested for the formation of filamentary features seen in A 3667 (Mazzotta et al. 2002). For 2A 0335+096, the detection of the 3.4 keV component in the central region and the 1.7 keV component for the cool tail supports this idea. In addition, we notice that there exists a filamentary excess structure northeast of the core observed by Chandra (see figure 12 of Mazzotta et al. 2003). The filamentary structure also favors turbulent viscous stripping.

According to Nulsen (1982), the mass-loss rate through turbulent viscous stripping is given by $\dot{M}_{\rm turb} \sim \pi R^2 \rho_{\rm ICM} v$, where R is the radius of the gas core, $\rho_{\rm ICM}$ is the density of the ambient ICM, and v is the relative velocity of the core with respect to the ICM. Referring to Mazzotta, Edge, and Markevitch (2003), we adopted values of $R = 40$ kpc and $v = 760\,{\rm km\,s^{-1}}$, which correspond to a Mach number of 0.8 for the 3.4 keV gas. As the core moves through the surrounding ICM with the electron density in the range of $\sim (2\text{–}7) \times 10^{-3}\,{\rm cm^{-3}}$ at $r \sim 1'.5$–$4'$, which was derived from the results of the referential region of $PA = 120°$–$210°$, the mass-loss rate would be $\dot{M}_{\rm turb} \sim 200\text{–}800\,M_\odot\,{\rm yr^{-1}}$. We then derived the mass-loss rate from our results.

Assuming that the 1.7 keV component obtained by the 2T model fit to the spectrum of the sector region (see table 6) is emission from the stripped cool gas, we estimated the mass-loss rate of the cool gas. From the 2T model fit, the APEC normalization of the 1.7 keV component is 2.42×10^{-3}. Given that the tail lies on the plane of the sky with the core, and the tail width along the line of sight is 63 kpc ($\approx 90''$), which is on the same scale as the apparent width, the volume of the tail is $V = 2.5 \times 10^{70}\,{\rm cm^3}$. Based on a further assumption that the 1.7 keV component is distributed uniformly in the entire volume of the tail, we derived an electron density of $n_{\rm e} = 5.6 \times 10^{-3}\,{\rm cm^{-3}}$. The gas mass contained in the volume, calculated from $1.2\,n_{\rm e}\,m_{\rm p}\,V$ ($m_{\rm p}$ is the proton mass), is then $1.4 \times 10^{11}\,M_\odot$. Using the velocity of the moving core, we calculate that the time taken for the core to cross the length of the trail in the sector region ($\simeq 190$ kpc) is 2.5×10^8 yr. If we assume that the gas mass has been accumulated during this time, we would estimate that the mass-loss rate to be $\dot{M} \sim 600\,M_\odot\,{\rm yr^{-1}}$. If the stripped gas is distributed in the filamentary form, the mass-loss rate would be reduced by a factor of $\sqrt{f}$, where f is a volume filling factor. For example, for a volume filling factor of $f = 0.5$, the reduced mass-loss rate is $\dot{M} \sim 400\,M_\odot\,{\rm yr^{-1}}$, which agrees with the estimated mass-loss rate due to the turbulent viscous stripping. Consequently, we argue that the soft tail feature can be produced by turbulent viscous stripping. At least it is reasonable to think that the spiral trail left behind the core points to the turnaround motion of the core, which has been suggested for other clusters, such as A 2142 (Markevitch et al. 2000), A 1795 (Markevitch et al. 2001), and A 3667 (Briel et al. 2004). Since the core motion in the ICM is decelerated by a drag force, we expect a damping oscillation of the core.

5.2. *Cold Front of A 496*

The most natural explanation for the southern cold front is the leading edge of a body of cold dense gas moving through the hotter ICM. Following a treatment described in Vikhlinin, Markevitch, and Murray (2001), we estimate the velocity of the moving body. We have shown that the sharp brightness edge is representative of a density jump of 1.27 ± 0.11. As shown in figure 19, the temperature on both sides of the density jump is consistent with a constant. Adopting the average values of the deprojected temperature in $r = 2'$–$4'$ and $r = 4'$–$7'.5$ and the amplitude of the density jump, we derived the ratio of the inside pressure to the outside pressure to be 0.90 ± 0.14, which is consistent with a continuous pressure across the jump. According to equation (2) in Vikhlinin, Markevitch, and Murray (2001), the corresponding Mach number of the body is less than ~ 0.2. Therefore, the body is moving at subsonic speed at most, and does not create a shock front ahead of it.

Using Chandra data, Dupke and White (2003) studied the gas profiles across the northern brightness edge $\sim 1'.5$ north of the X-ray emission peak, and showed that the profiles are consistent with the cold front characteristics. Our analysis of the XMM-Newton data has also revealed another cold front located $4'$ south of the X-ray emission peak. The two cold fronts are located at opposite sides of the X-ray brightness peak, which coincides with the cD galaxy. Among the clusters with two cold fronts, such as A 2142, RX J1720.1+2638, and A 2204 (Markevitch et al. 2000; Mazzotta et al. 2001; Sanders et al. 2005), these features are similar to the properties of RX J1720.1+2638.

There has been mainly three hypothesises for producing the cold fronts in clusters. First, as suggested by Markevitch et al. (2000) at first, the cold front may be the leading edge of the remaining core of a merged subcluster. Figure 5 in Markevitch et al. (2000) illustrates this scenario for the cluster A 2142 schematically. The second hypothesis is that the cold front is the result of an oscillating subhalo. This hypothesis was suggested by Mazzotta et al. (2001). In their scenario, the subhalo and larger halo are formed from two perturbations on different linear scales, but at almost the same place in the primordial density field. As the primordial density field evolves, the smaller-scale perturbation collapses first and forms the subhalo, while the larger-scale perturbation continues to evolve to form a more extended halo. The subhalo could have formed slightly offset from the center of the large halo, and is now falling into or oscillating around the center. This idea is supported by theoretical work. Fujita et al.

Downloaded from https://academic.oup.com/pasj/article/58/4/703/1456709 by Yildiz Teknik University Library (YTU) user on 25 February 2022

(2002) constructed an analytical model of the mass-distribution function of subhalos in a galaxy cluster, and estimated the probability of finding large X-ray subhalos. Their results imply that the observed cold fronts are not necessarily remnants of mergers. A third hypothesis also involves oscillation of the subhalo, which is triggered by the off-axis passage of a subcluster (Tittley, Henriksen 2005). In this scenario, the infall of a small gravitational substructure disturbs the central gravitational potential of the main cluster, and the cluster potential starts to oscillate. Tittley and Henriksen (2005) examined this hypothesis by comparing the simulated gas distribution and the X-ray surface-brightness profiles of several clusters observed by Chandra. In practice, they argued that the brightness edges seen in the central region of A 496 can be explained by the oscillation model.

In light of the 2D temperature profile for the outer region, we describe which hypothesis is the most plausible in the following section.

5.3. *Outer Non-Uniform Temperature Distribution*

Our investigation of the 2D temperature profile reveals a non-uniformity not only in the central region, but also in the outer region of $r > 5'$ for both 2A 0335+096 and A 496. Thus, the radial temperature profile of the outer region is the result of averaging over annuli with azimuthal temperature variations.

For A 496, while the radial temperature profile exhibits an increase toward the outside, we find patchy cool regions at $r \sim 5'$–$9'$ in the north and west directions. The map of the relative deviation of the surface brightness (figure 14) shows that the northwest excess region corresponds to the cool regions. An accordance between the positive deviation and the cool region has been seen for several clusters, such as the Perseus cluster (Churazov et al. 2003). Similarly in the case of the Perseus cluster, the global asymmetry of the gas temperature and the surface brightness distributions suggest that a merger has occurred in the direction of north-northwest to south-southeast. The linear north–south distribution of galaxies in the region of $r < 20'$ (Kriessler, Beers 1997) supports this idea. It is unlikely that the two oscillation models mentioned in the previous section would explain the asymmetric distribution on a cluster scale. Therefore, the most plausible interpretation of the two cold fronts is that the leading edge of the remaining core of a merged subcluster, namely, the northern (southern) cold front delineates the remnant of the merged subcluster that came from the south-southeast (north-northwest). The central morphology seen in the Chandra image (Tittley, Henriksen 2005) is probably related to the core oscillations induced by the merger. The patchy cool regions are most likely attributed to the stripped gas of the subcluster that came from the north-northwest.

For 2A 0335+096, we found the clockwise temperature increase in the outer region, from the southeast region of 3 keV to the southwest region of 3.6 keV. Although the temperature difference is very small compared with that seen in merging clusters, the temperature variation on the cluster scale suggests that this cluster experienced a merger in the past. The temperature variation would be smoothed out by thermal conduction. The timescale of thermal conduction over the scale l is given by $t_{\rm cond} \sim n_{\rm e}\, k_{\rm B}\, l^2/\kappa_{\rm s}$, where $n_{\rm e}$ is the electron density, $k_{\rm B}$ the Boltzmann constant, and $\kappa_{\rm s}$ the classical Spitzer conductivity. Adopting a scale of 400 kpc and an electron density of $\sim 5 \times 10^{-4}$ at $r \sim 9'$, we robustly estimate that the conduction timescale is $\sim 1 \times 10^9$ yr. This indicates that the merger occurred less than $\sim 1 \times 10^9$ yr ago. Thus, it is plausible to think that the moving core is the remaining core of a merged subcluster and the spiral cool tail left behind the core points to an off-set merger. Compared with A 496, we do not see any features of another cold front. We speculate that the other subcluster did not have a dense core that could survive the merger. The slightly cool southeast region might be a remnant of the other subcluster, which were decoupled from its dark matter after the merger and has been dispersed by ram pressure.

6. Conclusion

We have presented the results of the galaxy clusters 2A 0335+096 and A 496 observed by XMM-Newton. From an investigation of the 2D ICM profiles, we have obtained new features that are related to the dynamical structures of the ICM.

For 2A 0335+096, we found a spiral cool tail trailing behind the central cold core with respect to the core motion. This feature clearly shows a turnaround motion of the core. We speculate that the cool tail feature was produced by turbulent viscous stripping. For A 496, we found another cold front $4'$ south of the X-ray emission peak. A study of the gas profiles across the southern brightness edge has revealed a subsonic motion of the gas body. Regarding the temperature distribution in the outer region, we found non-uniformity for both clusters. The temperature variation on the cluster scale suggests the activity of a past merger. We argue that the dynamical gas motions seen in both clusters can be attributed to a past merger. Future measurements of the gas velocity along the line of sight will deepen our understanding of the dynamical structure and evolution of clusters of galaxies.

We would like to thank the XMM-Newton team for the spacecraft operation and calibration. This work was supported in part by a Grant-in-Aid for Specially Promoted Research (No. 15001002), from the Ministry of Education, Culture, Sports, Science and Technology (MEXT).

References

Anders, E., & Grevesse, N. 1989, Geochim. Cosmochim. Acta, 53, 197
Blanton, E. L., Sarazin, C. L., & McNamara, B. R. 2003, ApJ, 585, 227
Briel, U. G., Finoguenov, A., & Henry, J. P. 2004, A&A, 426, 1
Churazov, E., Forman, W., Jones, C., & Böhringer, H. 2003, ApJ, 590, 225
Churazov, E., Gilfanov, M., Forman, W., & Jones, C. 1999, ApJ, 520, 105
David, L. P., Jones, C., Forman, W., & Daines, S. 1994, ApJ, 428, 544

Downloaded from https://academic.oup.com/pasj/article/58/4/703/1456709 by Yildiz Teknik University Library (YTU) user on 25 February 2022

de Plaa, J., Kaastra, J. S., Tamura, T., Pointecouteau, E., Mendez, M., & Peterson, J. R. 2004, A&A, 423, 49
den Herder, J. W., et al. 2001, A&A, 365, L7
Dickey, J. M., & Lockman, F. J. 1990, ARA&A, 28, 215
Dupke, R., & White, R. E., III 2003, ApJ, 583, L13
Fabian, A. C., Ku, W. H.-M., Malin, D. F., Mushotzky, R. F., Nulsen, P. E. J., & Stewart, G. C. 1981, MNRAS, 196, 35p
Fabian, A. C., Sanders, J. S., Ettori, S., Taylor, G. B., Allen, S. W., Crawford, C. S., Iwasawa, K., & Johnstone, R. M. 2001, MNRAS, 321, L33
Fujita, Y., Sarazin, C. L., Nagashima, M., & Yano, T. 2002, ApJ, 577, 11
Furusho, T., et al. 2001, PASJ, 53, 421
Gunn, J. E., & Gott, J. R., III 1972, ApJ, 176, 1
Irwin, J. A., & Sarazin, C. L. 1995, ApJ, 455, 497
Jansen, F., et al. 2001, A&A, 365, L1
Kaastra, J. S., et al. 2004, A&A, 413, 415
Kaastra, J. S., Ferrigno, C., Tamura, T., Paerels, F. B. S., Peterson, J. R., & Mittaz, J. P. D. 2001, A&A, 365, L99
Kaastra, J. S., Lieu, R., Tamura, T., Paerels, F. B. S., & den Herder, J. W. 2003, A&A, 397, 445
Katayama, H., Takahashi, I., Ikebe, Y., Matsushita, K., & Freyberg, M. J. 2004, A&A, 414, 767
Kawano, N., Ohto, A., & Fukazawa, Y. 2003, PASJ, 55, 585
Kriessler, J. R., & Beers, T. C. 1997, AJ, 113, 80
Markevitch, M., et al. 2000, ApJ, 541, 542
Markevitch, M., Vikhlinin, A., & Forman, W. R. 2003, ASP Conf. Ser., 301, 37
Markevitch, M., Vikhlinin, A., & Mazzotta, P. 2001, ApJ, 562, L153
Mazzotta, P., Edge, A. C., & Markevitch, M. 2003, ApJ, 596, 190
Mazzotta, P., Fusco-Femiano, R., & Vikhlinin, A. 2002, ApJ, 569, L31
Mazzotta, P., Markevitch, M., Vikhlinin, A., Forman, W. R., David, L. P., & VanSpeybroeck, L. 2001, ApJ, 555, 205
Nulsen, P. E. J. 1982, MNRAS, 198, 1007
Peterson, J. R., et al. 2001, A&A, 365, L104
Read, A. M., & Ponman, T. J. 2003, A&A, 409, 395
Romanishin, W., & Hintzen, P. 1988, ApJ, 324, L17
Sanders, J. S., Fabian, A. C., & Taylor, G. B. 2005, MNRAS, 356, 1022
Sarazin, C. L., Baum, S. A., & O'Dea, C. P. 1995, ApJ, 451, 125
Smith, R. K., Brickhouse, N. S., Liedahl, D. A., & Raymond, J. C. 2001, ApJ, 556, L91
Strüder, L., et al. 2001, A&A, 365, L18
Tamura, T., et al. 2001a, A&A, 365, L87
Tamura, T., Bleeker, J. A. M., Kaastra, J. S., Ferrigno, C., & Molendi, S. 2001b, A&A, 379, 107
Tanaka, Y., Inoue, H., & Holt, S. S. 1994, PASJ, 46, L37
Tittley, E. R., & Henriksen, M. 2005, ApJ, 618, 227
Turner, M. J. L., et al. 2001, A&A, 365, L27
Vikhlinin, A., Markevitch, M., & Murray, S. S. 2001, ApJ, 551, 160
Watanabe, M., Yamashita, K., Furuzawa, A., Kunieda, H., & Tawara, Y. 2001, PASJ, 53, 605
Watanabe, M., Yamashita, K., Furuzawa, A., Kunieda, H., Tawara, Y., & Honda, H. 1999, ApJ, 527, 80
Werner, N., de Plaa, J., Kaastra, J. S., Vink, J., Bleeker, J. A. M., Tamura, T., Peterson, J. R., & Verbunt, F. 2006, A&A, 449, 475

Downloaded from https://academic.oup.com/pasj/article/58/4/703/1456709 by Yildiz Teknik University Library (YTU) user on 25 February 2022